

CFD MODELLING OF GAS FLOW CHARACTERISTICS FOR THE GAS-HEATING HOLDER IN ENVIRONMENTAL TRANSMISSION ELECTRON MICROSCOPE

Zhijian Zhao,^{1,2} Zhiyong Wang,^{1,2} Dan Wang,^{1,2*} Jie-Xin Wang,¹ Yuan Pu^{1,2*} and Jian-Feng Chen^{1,2}

1. Research Centre of the Ministry of Education for High Gravity Engineering Technology, Beijing University of Chemical Technology, Beijing 100029, China

2. State Key Laboratory of Organic-Inorganic Composites, Beijing University of Chemical Technology, Beijing 100029, China

The environmental transmission electron microscope (ETEM) is an effective tool for understanding the behaviour of materials at an atomic level. In the present work, we have characterized the dynamics of gas flow in ETEM using computational fluid dynamic (CFD) simulations. The gas pressure drop, pressure distribution, and gas flow of different inlet pressures for a gas chamber are investigated. Based on the detailed CFD simulations, the hydrodynamics for the gas-heating holder are carried out. Also, an attempt has been made to optimize the structure, and it is proposed that the triangle shaped inlet tube is more suitable. The results presented are useful for understanding the dynamics of gas flow in a gas chamber and provide a basis for further structure optimizations.

Keywords: environmental TEM, gas-heating holder, CFD, gas flow simulation

INTRODUCTION

In recent years, understanding the behaviour of materials at an atomic level has attracted tremendous attention in both academic and industrial research.^[1–5] Much focus has been given to the development of microscopic imaging equipment, such as transmission electron microscopy (TEM),^[6–9] scanning electron microscopy (SEM),^[10–12] atomic force microscope (AFM),^[13,14] laser scanning confocal microscopy (LSCM),^[15–17] and stimulated emission depletion microscopy (STED).^[18,19] Among them, the environmental transmission electron microscope (ETEM),^[20,21] which introduces a gas or liquid atmosphere around the sample chamber of a TEM, is a valuable technique to investigate the gas-solid or liquid-solid interactions at a nanometer scale. The ETEM can also be used to perform in situ synthesis of nanomaterials to obtain the knowledge of the time- and temperature-resolved dynamic and kinetic mechanisms at near-atomic resolution.^[22,23] For instance, Hitachi has developed a 300 kV high-resolution H-9500 TEM with gas injection/heating capability by using a gas injection/specimen heating holder.

As a nanolabatory for the synthesis and characterization of nanomaterials, comprehensive understanding of the gas flow characteristics for the gas-heating holder in ETEM is needed, because the behaviours of the gas-solid reactions are usually influenced by the gas pressure and temperature distribution. However, it is difficult to obtain the gas flow characteristics for the gas-heating holder in the ETEM by using empirical correlations of experimental data. Computational fluid dynamics (CFD) is an independent discipline based on the classical hydrodynamics and numerical calculation method, which describes the numerical solution of the flow field quantitatively.^[24,25] The CFD has been applied in environmental flows to deal with the issues of gaseous pollutant dispersion,^[26–29] mechanical design to optimize equipment performance,^[30–33] the performance of volatile biomass combustion or gasification system,^[34–36] emerging as a powerful and effective tool to simulate the hydrodynamics and mass transfer behaviour of various processes.^[37–39]

In this article, a three-dimensional CFD model with the same structure and size as a commercially available Hitachi gas-heating holder is developed to describe the gas flow simulation of the holder in ETEM at room temperature. The gas pressure drop, pressure distribution, and gas flow of different inlet pressures were investigated. We also performed structural optimization, such as inlet position and shape of tube. The 3D physical model describing the actual gas-heating holder in ETEM gave a deep understanding of the gas flow behaviour around the sample. The obtained knowledge of the hydrodynamics for the gas-heating holder is also instructive for the holder design, optimization, and performance.

EXPERIMENTAL SECTION

Structure of a Gas-Heating Holder

A practicality photo and the structure parameters of a gas-heating holder for Hitachi H-9500 TEM are presented in Figure 1. The main part of the holder consists of a spiral-shaped wire of tungsten (W) and a gas injection nozzle made of alloy. For in situ experiments, the powder sample was coated on the surface of the W wire, and then observed in the ETEM system. By adjusting the intensity of the electrical current that flows through the W wire, the temperature of the sample could be controlled from room temperature to as high as 1500 °C. Gases including N₂, H₂, O₂, air, water vapour, and others could be introduced to the sample from the gas injection nozzle. In our simulation, the specimen chamber was the same as the real one shown in Figure 1.

* Authors to whom correspondence may be addressed.
E-mail addresses: wangdan@mail.buct.edu.cn (D. Wang)
or puyuan@mail.buct.edu.cn (Y. Pu).
Can. J. Chem. Eng. 97:777–784, 2019
© 2018 Canadian Society for Chemical Engineering
DOI 10.1002/cjce.23217
Published online 30 March 2018 in Wiley Online Library
(wileyonlinelibrary.com).

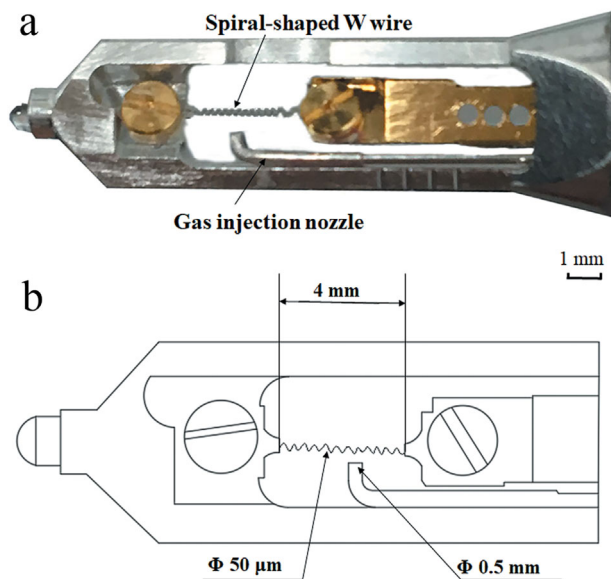


Figure 1. The sketch of gas injection-heating sample holder.

Mathematical Modelling

The governing equations for this simulation are the continuity, the momentum, and the energy equation. The continuity and momentum equations can be expressed as follows:^[40]

$$\frac{\partial u_i}{\partial x_i} = 0 \quad (1)$$

$$\rho \frac{\partial u_i}{\partial x_i} + \rho \frac{\partial u_i u_j}{\partial x_j} = -\rho \frac{\partial p}{\partial x_i} + \rho \frac{\partial}{\partial x_i} \left(\mu \rho \frac{\partial u_i}{\partial x_i} + \rho \tau_{ji} \right) \quad (2)$$

where u is the velocity of the flow, ρ is the density, p is the pressure, μ is the viscosity, and τ_{ij} is the Reynolds stress, it equals that:

$$\tau_{ij} = \tau_{ji} = -\overline{u'_i u'_j} \quad (3)$$

The Reynolds stress can be calculated as the following equation:

$$\rho \overline{u'_i u'_j} = -\mu_t \left(\frac{\partial u_i}{\partial x_j} + \frac{\partial u_j}{\partial x_i} \right) + \frac{2}{3} \rho k \quad (4)$$

$$\mu_t = C_\mu \rho k^2 / \varepsilon \quad (5)$$

where $C_\mu = 0.09$, μ_t is the turbulent viscosity, k is the turbulence kinetic energy, and ε is turbulence dissipation, both can be gained from the following formulae:

$$\frac{\partial}{\partial t} (\rho k) + \frac{\partial}{\partial x_i} (\rho u_i k) = \frac{\partial}{\partial x_j} \left[\left(\mu + \frac{\mu_t}{\sigma_k} \right) \frac{\partial k}{\partial x_j} \right] + G_k - \rho \varepsilon \quad (6)$$

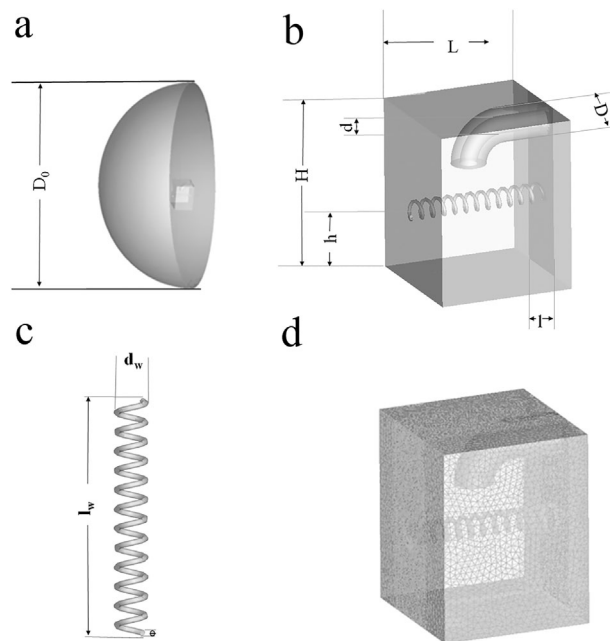


Figure 2. Representation of schematics and grid of simulation model. (a) 3D view of the whole system; (b) 3D view of the specimen chamber; (c) 3D view of the tungsten filament; and (d) 3D view of CFD grids of the specimen chamber.

$$\frac{\partial}{\partial t} (\rho \varepsilon) + \frac{\partial}{\partial x_i} (\rho u_i \varepsilon) = \frac{\partial}{\partial x_j} \left[\left(\mu + \frac{\mu_t}{\sigma_\varepsilon} \right) \frac{\partial \varepsilon}{\partial x_j} \right] + C_{1\varepsilon} \frac{\varepsilon}{k} - C_{2\varepsilon} \frac{\varepsilon^2}{k} \rho \quad (7)$$

where G_k is the generation of turbulence kinetic energy due to the mean velocity gradients shown as follows:

$$G_k = \mu_t \left(\frac{\partial u_j}{\partial x_i} + \frac{\partial u_i}{\partial x_j} \right) \frac{\partial u_i}{\partial x_j} \quad (8)$$

Boundary Conditions and Simulation Strategy

Figure 2 shows the geometry and notations of the specimen chamber and Table 1 gives their values. A three-dimensional grid was created using ANSYS ICEM-CFD 17.1. Three types of grids with different numbers of cells were tested, containing 389 862, 1 389 738, and 2 821 142, respectively, in order to choose the optimum grid number. The difference was less than 5 % for all variables examined, suggesting that the computed results were independent of the characteristics of the mesh size.

RESULTS AND DISCUSSION

Model Validation

The pressure distribution is the most important parameter for the specimen chamber and is used as the primary parameter to

Table 1. Parameters of the simulation model

D_0 (mm)	H (mm)	L (mm)	h (mm)	l (mm)	D (mm)	d (mm)	d_w (mm)	l_w (mm)	Φ (mm)
20	5	4	2	1.7	1	0.5	0.5	4	0.1

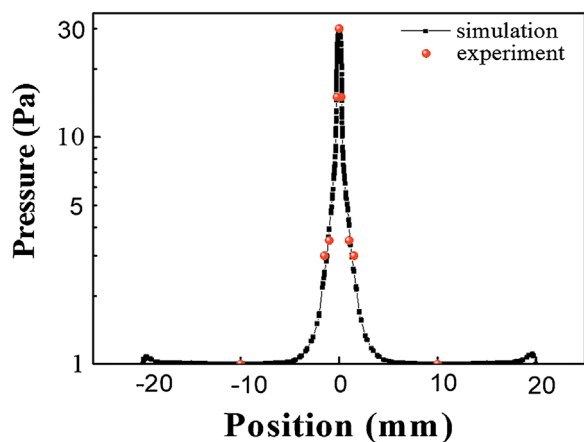


Figure 3. Comparison between the simulated and measured pressure at different positions.

revise the simulation in this work. Figure 3 shows the simulated pressure at different positions and the experimental results from the specification. Figure 3 shows that the simulation data is in good accordance with the experimental ones. Therefore, the simulation results can be verified, and all the latter works are based on that. In addition, Figure 3 also gives information that the peak value appears in the top surface of the tungsten filament, and the pressure decrease with the increase of distance; this is relevant to the block of tungsten filament to the flow gas. Only when the distance is larger than 3 mm can the pressure get stable, which is measured as operating pressure, but the narrow region near the original point is where the sample coated and it is much larger than operating pressure. So, it is necessary to explore the actual pressure of the region near the filament where the sample is located.

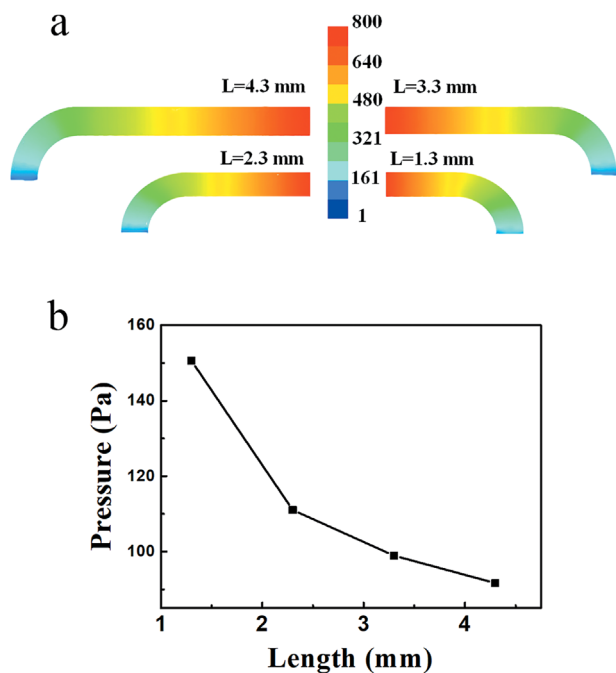


Figure 4. (a) Distributions of pressure varying the length of tube; and (b) out pressures of different length.

Gas Flow Patterns

Different operating pressure (OP)

For the purpose of reducing computation workload, the simulation is simplified, and rationality is discussed. It is well known that the gas flow rate is proportional to the gas pressure. However, from the source gas to the specimen chamber, the pressure has a tremendous loss because of both the pressure-regulating system and the resistance loss in the tube, and the latter is simulated in this work. We vary the length of straight pipe from 1.3–4.3 mm; the result is shown in Figure 4. From Figure 4a, we can get that pressure drop mostly in the bent place. Figure 4b exhibits how the increase of 3 mm makes a big difference to outlet pressure; however, the real tube is over 40 cm long. Therefore, calculating from the gas source requires great effort and it is not very meaningful, so we calculate from part of the tube and focus on the operating pressure, which can be read on the display screen. Based on that, once the operating pressure is detected, we can know how the pressure distributes and what it is like in the flow field for the other parameters like velocity and density.

One operating parameter of ETEM is the operating pressure, so the influence of operating pressure is necessary. Figure 5a shows the comparison of pressure distribution under different operating pressures. All the peak values appear on the wall surface of tungsten filament, and the pressure drops sharply near the filament. As the

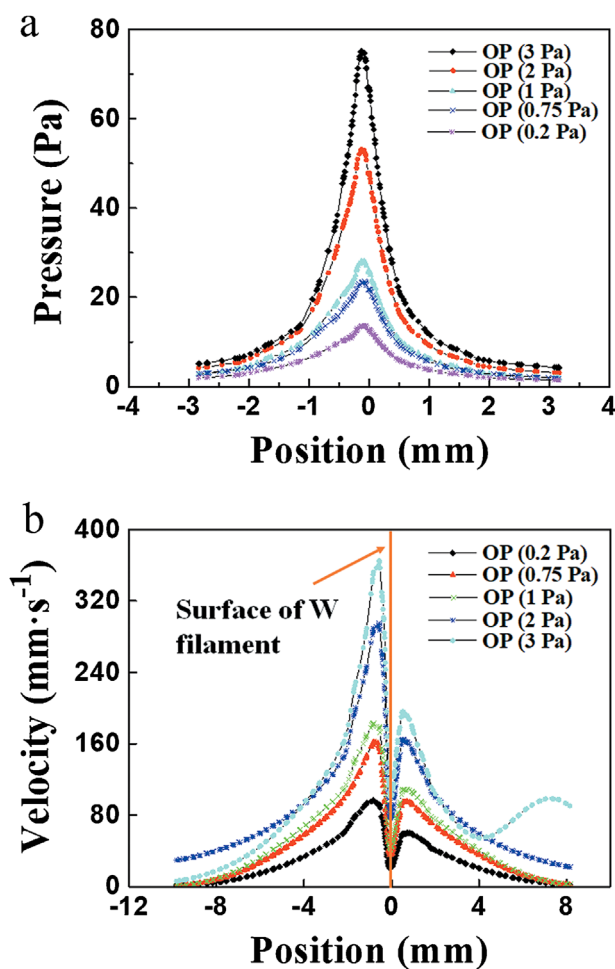


Figure 5. (a) Comparison of pressure distribution under different operating pressures; and (b) comparison of velocity distribution under different operating pressures.

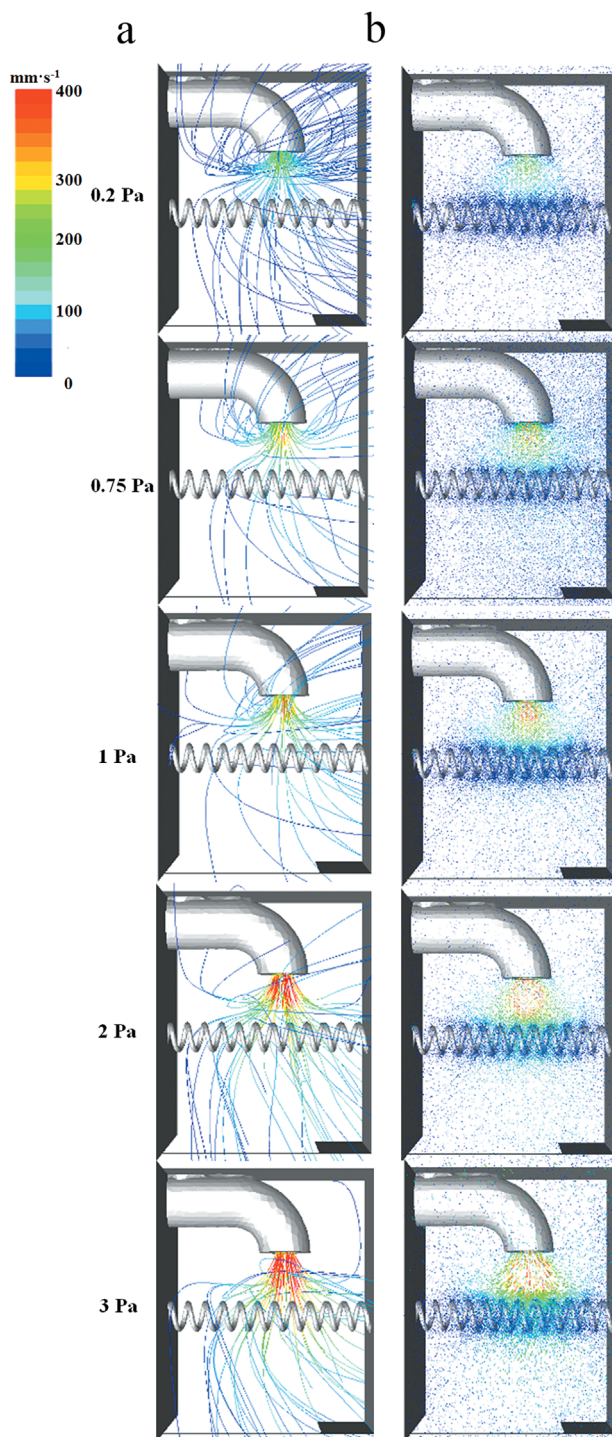


Figure 6. (a) Comparison of path lines between different operating pressures; and (b) comparison of vectors between different operating pressures.

operating pressure increases, the rapid increase of peak value is shown. Even in the high vacuum condition, the local pressure can be huge, which can damage the atomic resolution imaging. Our work may offer some insight into the necessary balance between the actual pressure and the resolution imaging needs.

A major concern when heating the samples observed in situ is how to keep the specimen stable, and the key to reach this requirement is to lower the drift of the specimen, so that the velocity in the flow field is also considered. Figure 5b gives the

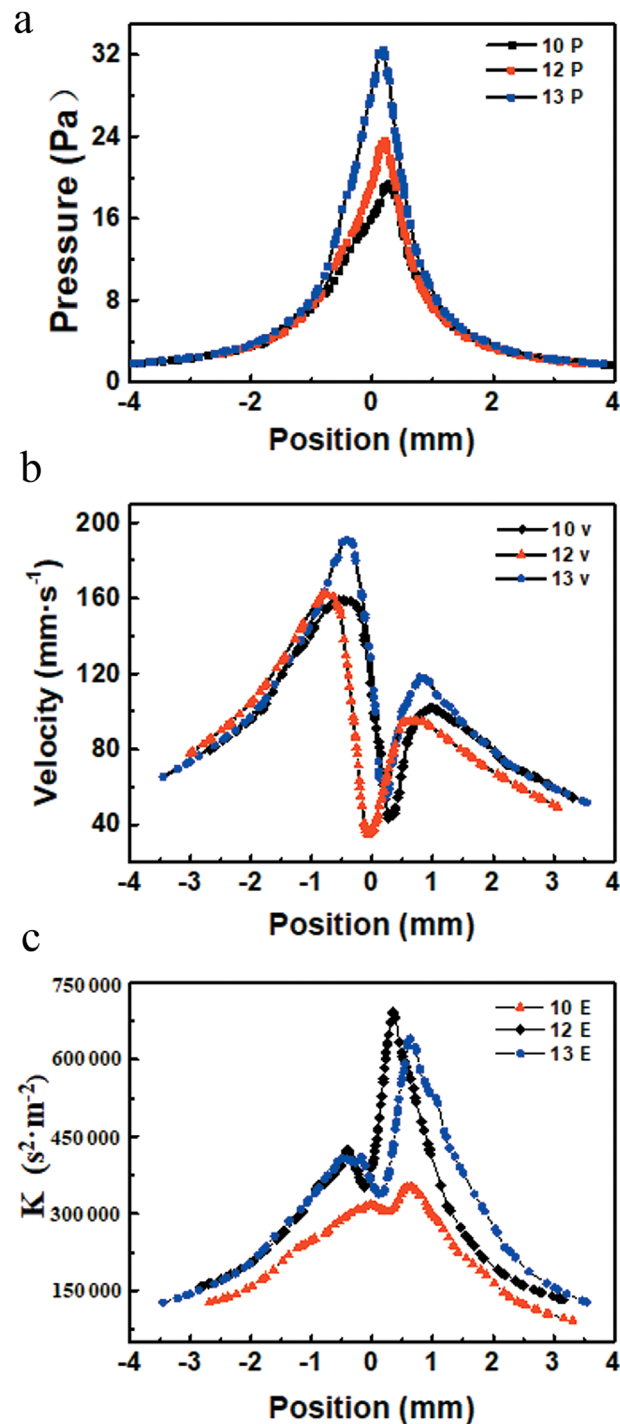


Figure 7. Comparison of parameters between different screw pitches: (a) pressure; (b) velocity; and (c) turbulent kinetic energy.

graphical representation of velocity. Because the inlet tube is not pointed directly to the centre of the filament, the velocity contribution is not symmetrical (which is different from the pressure), and the tube side shows a larger velocity. Like pressure contribution, the velocity near the W filament gets its peak and is more sensitive, but with a stagnant layer probably because of the block of the wall surface, and the layer gets thinner with the increase in operating pressure.

More details about the flow are shown as Figure 6. Figure 6a shows that with a lower inlet pressure, quite a large part of fluid flow goes backward, and as the operating pressure

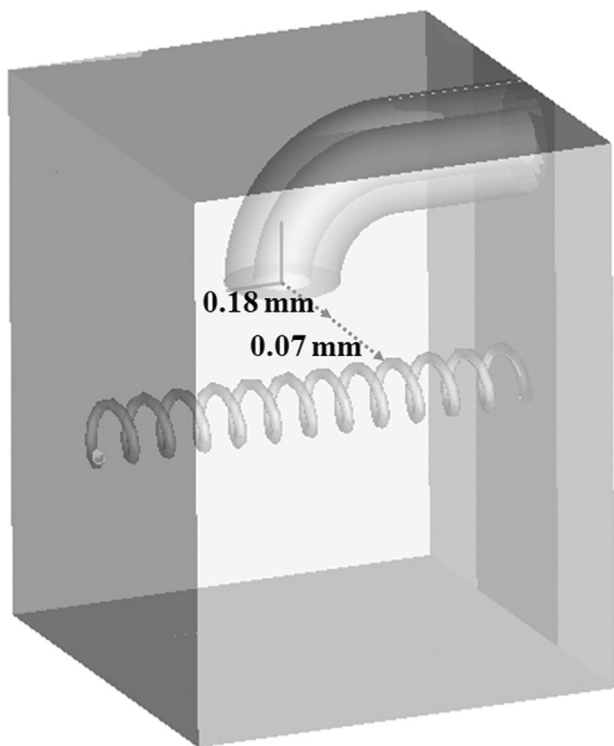


Figure 8. Representation of inlet position variations.

increases, this proportion reduces clearly. So, under a lower operating pressure, the pressure-driven flow is much weaker, and more susceptible to wall blocking. From Figure 6b we can get the distribution of the gases, and under the different conditions, they all show a stagnant zone near the W filament, which agrees with Figure 5b. This stagnant zone is because of the helically-wound tungsten filament, which is designed to minimize the draft rate.

Different screw pitch

Besides the pressure inlet, the screw pitch is another parameter that can be operated. As we discuss above, the structure of the W filament has many functions, so it is necessary to get a further analysis about that. In this work, we change the number of turns in the fixed distance of 4 mm to explore the effects of screw pitch, with 10, 12, and 13 turns. In addition, parameters like pressure, velocity, and turbulent kinetic energy are chosen to evaluate the effect of screw pitch, as shown in Figure 7. Figure 7a shows that with the same operating pressure, the peak value can get higher when the screw pitch is narrowed. Also, the result is applicable to the velocity distribution, because when the screw pitch narrows, the role of block effect is more evident. On the observation of nanomaterials in situ by ETEM, a major concern is how to keep the specimen stable in order to lower the drift. The turbulent kinetic energy (k) is a parameter that reflects the turbulence of flow, which is defined as follows:

$$k = \frac{1}{2} \times m \times v^2 \quad (9)$$

where m , v' are, respectively, quality and turbulent velocity. Here, the turbulent kinetic energy is the sum of the kinetic energy ($\sum_{cell=1}^{cell\ number} (\frac{1}{2} m_{cell} v_{cell}^2)$) in each computational cell,^[41] and

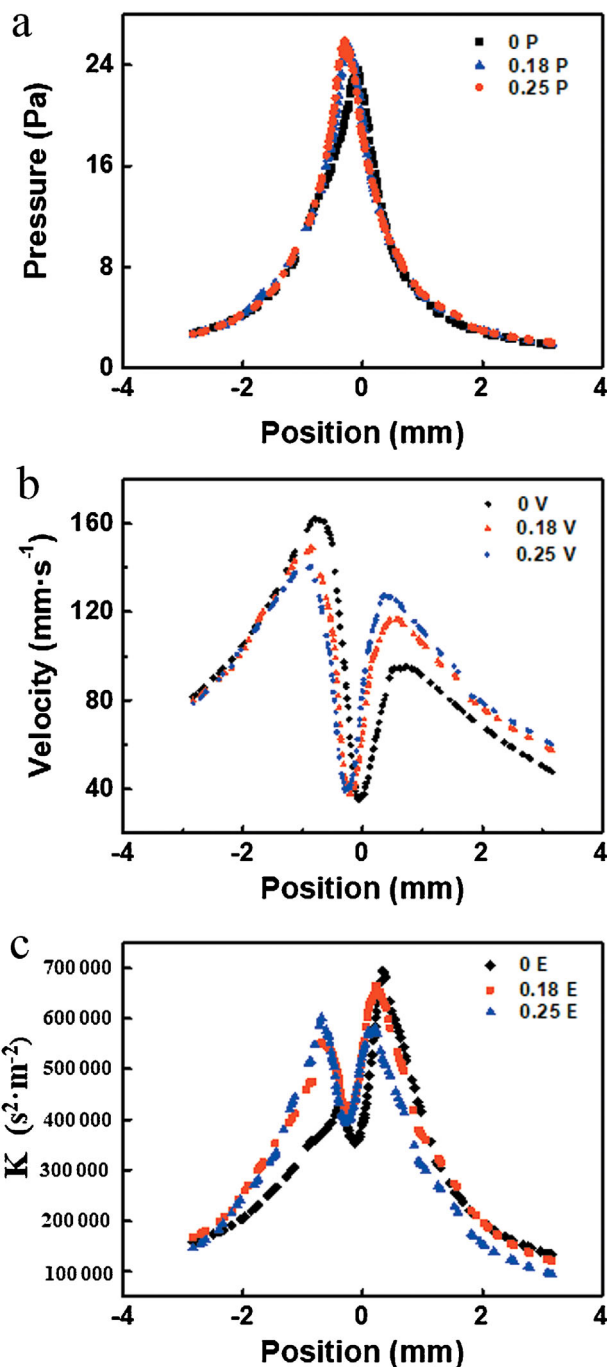


Figure 9. Comparison among different inlet pitches: (a) pressure; (b) velocity; and (c) turbulent kinetic energy.

there is a relationship between the turbulent kinetic energy and the turbulent intensity:

$$k = \frac{3}{2} \times (u \times l)^2 \quad (10)$$

where u and l are mean velocity and turbulent intensity, respectively, so we can evaluate the stability of the flow field by comparing the value of k .

Figure 7c shows that as the screw pitch gets larger, the turbulent kinetic energy (k) gets smaller accordingly. Note especially that the peak appears at the opposite side of the velocity peak, possibly

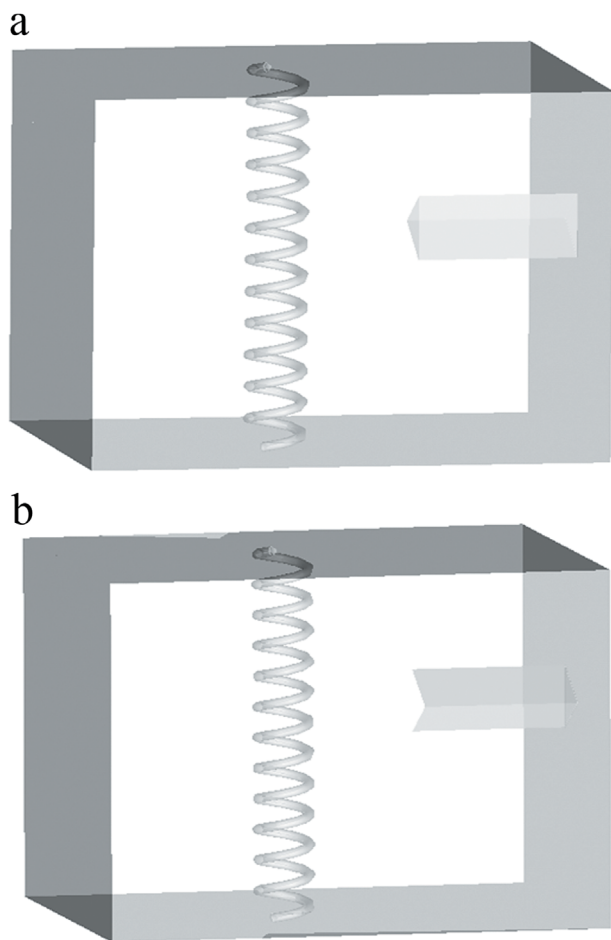


Figure 10. Schematic of the different shapes of inlet tube: (a) triangle (Δ); and (b) inverted triangle (∇).

because flow around the filament can cause a more violent turbulence. Hence, the top side of the filament is more suitable to hold the specimen, and the screw pitch should be bigger, so that we can get the sample with lower disturbance.

Structure Optimization

According to the discussion above, the behaviour of flow is governed by the relative position between the intake tube and the W filament, so the optimization of the inlet tube can markedly improve the stability and the utilization of the gas flow. Here we discuss the variation of the inlet position and the shape of the tube to inspect the differences among them, so as to get a deeper understanding of the structure and optimize the design.

Position of the inlet tube

As discussed before, the original tube is not pointing to the axial centre of the filament, so the meaning behind this design is explored. In this work, with other settings fixed, only the horizontal distance is adjusted as 0 (original), 0.18, and 0.25 mm, which is shown in Figure 8. Also, the pressure, velocity, and turbulent kinetic energy are chosen to weigh the pros and cons.

To investigate the differences among horizontal distances in quantification, Figure 9 gives the parameters that concern us and shows the pressure drift with the moving of the tube and the pressure getting a little higher. However, the velocity of the tube

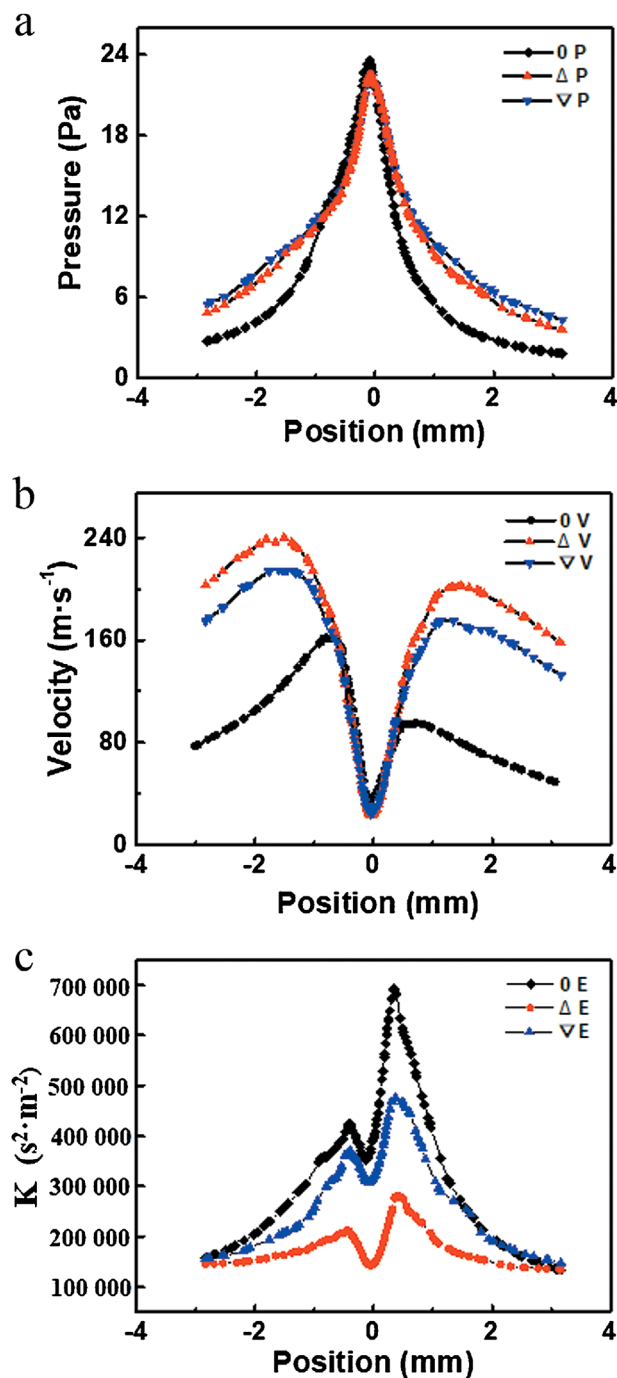


Figure 11. Comparisons of different inlet tube shapes: (a) pressure; (b) velocity; and (c) turbulent kinetic energy.

side gets lower, but with another side getting higher, which is opposite to turbulent kinetic energy. Therefore, the block effect of filament gets bigger with the horizontal moving of the inlet tube, which makes the pressure higher, and more gas can flow around the tube, balancing the distribution of velocity and turbulent kinetic energy. All in all, a design of a shorter distance between tube and filament will cause a rise in pressure, velocity, and turbulent kinetic energy in the region of the filament, which is harmful to imaging quality and the stability of samples. Thus, staggering the positions between the inlet tube and filament is a reasonable and necessary choice.

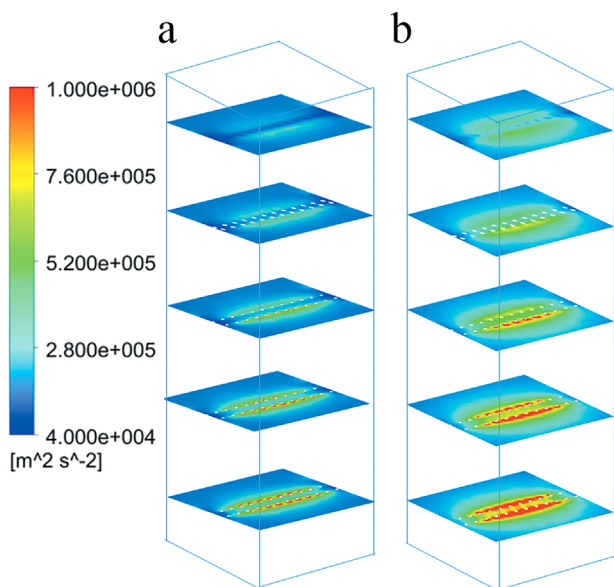


Figure 12. Distribution of turbulent kinetic energy near the W filament: (a) triangle (Δ); and (b) inverted triangle (∇).

Shape of the inlet tube

From the discussion of dislocation between the inlet tube and filament, we also get that the distribution of gas out the tube can affect the motion of gas. So, we remould the shape of tube to redistribute the gas flow. Shown as Figure 10, the shape of the inlet tube is designed as a triangle (Δ) and inverted triangle (∇). Here, we ignore the resistance loss of the bent, and the two types of triangle are chosen to examine the influence of the asymmetry of gas flow, which may give us guidance for further exploration.

Figure 11a gives comparisons of the different tube shapes by the distribution of pressure; the sample region shows no apparent difference, but the operating pressure in the other area is much higher than the original circle shape. That means with the same degree of vacuum, the sample area can also reach a relatively high degree. It should be noted that the simulation of the triangle-shaped tube does not consider the bending resistance loss, making the pressure and velocity of the flow field higher than the original design. Between the two new shape tubes, the triangle shape has a greater portion of gas contact with the filament directly, so the velocity near the filament can be bigger, but the turbulent kinetic energy is much lower than the inverted triangle one.

To investigate the differences for the whole flow field, the 3D view of the distribution of turbulent kinetic energy is shown in Figure 12. From the figure, we can see that the turbulent kinetic energy of the triangle-shaped inlet tube is significantly lower than the inverted triangle. This difference can be explained by the fact that more gas flows around the tungsten filament without colliding with it, which is same mechanism as the design of staggering the tube and filament. Therefore, in the narrow area of the sample holder, the inlet tube shaped as a triangle has some advantages over the circular one in minimizing turbulent fluctuation and the drift of the specimen.

CONCLUSION

A simulation has been made to describe the ideal gas flow under vacuum conditions in the specimen chamber of ETEM. Its validity

can be verified by information from the specification. Moreover, a visual view of path lines and distribution supports the explanations. The flow pattern in the chamber has been exhibited and the effect of inlet pressure, screw pitch, inlet position, and the tube shape are also analyzed in this work, leading to the following conclusions.

As the pressure of the inlet increases, the pressure of the whole field gets higher, and the maximum value appears at the surface of the filament. Also, the increase of pressure decreases the backflow blocked by the filament, and the helical structure of the filament can reduce the gas turbulence, which is helpful to form a stable atmosphere for the specimen on filament.

When the screw pitch gets smaller, only the flow near the filament can be affected, but it also leads to the increase in the turbulence, which can intensify the drift of the specimen. So, the screw pitch needs to get bigger to satisfy the practical requirements. The top surface of the filament is the best choice to place the sample that has the minimum velocity and turbulence.

Adjusting the inlet tube location towards the filament horizontally, we found that the pressure, velocity, and turbulent kinetic energy get raised in the region of the filament, and the peak moves accordingly. So, the design of the staggering tube and the filament is reasonable to prevent the reducing of vacuum in the sample region.

Trying to explore how the unsymmetrical distribution of the inlet gas flow affects the flow field, we designed a triangle-shaped tube. By comparing parameters like velocity and turbulent kinetic energy, we can show that the triangle-shaped inlet tube can effectively minimize turbulent fluctuation and the drift of the specimen. It may give another optional choice in the actual design.

This work developed a comprehensive understanding of the flow in ETEM, and also gave some enlightenment to optimize the chamber. However, it should be pointed out that ETEM can also heat the sample in situ, and that combining the gas flow with electrical heating by filament will give some more meaningful information. Therefore, more systematic studies are necessary to understand the details of observation in situ and hence generate results useful to application.

ACKNOWLEDGEMENTS

We are grateful for financial support from the National Key Research and Development Program of China (2017YFB0404302/2017YFB0404300), National Natural Science Foundation of China (21620102007 and 21622601), Beijing Natural Science Foundation (2182051), Fundamental Research Funds for the Central Universities (BUCTRC201601), and the “111” project of China (B14004).

REFERENCES

- [1] B. Li, Y. Kawakita, Y. Liu, M. Wang, M. Matsuura, K. Shibata, S. Ohira-Kawamura, T. Yamada, S. Lin, K. Nakajima, S. Liu, *Nat. Commun.* 2017, 8, 16086.
- [2] S. J. Chen, C. Y. Li, Q. Wang, W. H. Duan, *Carbon* 2017, 114, 557.
- [3] B. J. Siwick, J. R. Dwyer, R. E. Jordan, *Science* 2015, 302, 1382.
- [4] Z. Wang, R. Su, D. Wang, J. Shi, J.-X. Wang, Y. Pu, J.-F. Chen, *Ind. Eng. Chem. Res.* 2017, 56, 13610.
- [5] J. Xu, I. Jeon, J. Ma, Y. Dou, S. Kim, J. Seo, H. Liu, S. Dou, J.-B. Baek, L. Dai, *Nano Res.* 2017, 10, 1268.

- [6] C. Gong, K. He, G. D. Lee, Q. Chen, A. W. Robertson, E. Yoon, S. Hong, J. H. Warner, *ACS Nano* **2016**, *10*, 9397.
- [7] D. Wang, Z. Wang, Q. Zhan, Y. Pu, J.-X. Wang, N. R. Foster, L. Dai, *Engineering* **2017**, *3*, 402.
- [8] D. Wang, L. Zhu, Y. Pu, J.-X. Wang, J.-F. Chen, L. Dai, *Nanoscale* **2017**, *9*, 11214.
- [9] J. Xu, I. Jeon, H. Choi, S. Kim, N. Park, L. Dai, J.-B. Baek, *2D Mater.* **2017**, *4*, 014002.
- [10] M. Kopycinska-Mueller, J. Gluch, B. Köhler, *Nanotechnology* **2016**, *27*, 454001.
- [11] A. Jayalakshmi, I.-C. Kim, Y.-N. Kwon, *Chinese J. Chem. Eng.* **2017**, *25*, 931.
- [12] J. Liu, D. Wang, M. Wang, D. Kong, Y. Zhang, J.-F. Chen, L. Dai, *Chem. Eng. Technol.* **2016**, *39*, 891.
- [13] D. Wang, J. Liu, J.-F. Chen, L. Dai, *Adv. Mater. Interfaces* **2016**, *3*, 1500439.
- [14] E.-S. Jo, X. An, P. G. Ingole, W.-K. Choi, Y.-S. Park, H.-K. Lee, *Chinese J. Chem. Eng.* **2017**, *25*, 278.
- [15] Y. Wang, R. Hu, W. Xi, F. Cai, S. Wang, Z. Zhu, R. Bai, J. Qian, *Biomed. Opt. Express* **2015**, *6*, 3783.
- [16] D. Wang, L. Zhu, J.-F. Chen, L. Dai, *Nanoscale* **2015**, *7*, 9894.
- [17] D. Wang, L. Zhu, C. McCleese, C. Bruda, J.-F. Chen, L. Dai, *RSC Adv.* **2016**, *6*, 41516.
- [18] V. Giuseppe, T. Haisen, H. Alf, V. Mueller, M. P. Clausen, W. Dominic, S. Galiani, E. Sezgin, A. Diaspro, S. W. Hell, C. Eggeling, *Nano Lett.* **2015**, *15*, 5912.
- [19] Q. Zhan, H. Liu, B. Wang, Q. Wu, R. Pu, C. Zhou, B. Huang, X. Peng, H. Ågren, S. He, *Nat. Commun.* **2017**, *8*, 1058.
- [20] M. R. Ward, B. Theobald, J. Sharman, *J. Microsc.* **2017**, *269*, 143.
- [21] Y. Pan, J. Wu, X. Yin, H. Yang, *AIChE J.* **2016**, *62*, 399.
- [22] T. Kawasaki, H. Murase, K. Y. T. Tanji, *Phys. Rev. Lett.* **2015**, *58*, 1551.
- [23] C. D. Damsgaard, L. D. Duchstein, I. Sharafutdinov, *Microscopy* **2014**, *63*, 397.
- [24] M. Mohajerani, M. Mehrvar, F. E. Mozaffari, *Can. J. Chem. Eng.* **2015**, *90*, 1612.
- [25] N. Mao, M. Song, M. Chan, D. Pan, S. Deng, *Appl. Energ.* **2016**, *164*, 906.
- [26] W. J. A. Nahari, M. F. F. E. Dosoky, M. M. Abdelghany, *Chem. Eng. Sci.* **2016**, *44*, 54.
- [27] R. J. G. Lopes, R. M. Quinta-Ferreira, *Chem. Eng. Sci.* **2010**, *65*, 291.
- [28] S. Chen, Y. Fan, Z. Yan, W. Wang, C. Lu, *Powder Technol.* **2016**, *287*, 29.
- [29] J. Gan, Z. Zhou, A. Yu, *AIChE J.* **2016**, *62*, 62.
- [30] A. Kazemzadeh, F. Ein-Mozaffari, A. Lohi, L. Pakzad, *Can. J. Chem. Eng.* **2016**, *94*, 2394.
- [31] D. De Kee, D. Rice, C. Leissing, B. Meng, *Can. J. Chem. Eng.* **2016**, *94*, 1442.
- [32] D. Li, A. Buffo, W. Podgorska, D. L. Marchisio, Z. Gao, *Chinese J. Chem. Eng.* **2017**, *25*, 1369.
- [33] L. Raynal, C. Boyer, J. P. Ballaguet, *Can. J. Chem. Eng.* **2010**, *82*, 871.
- [34] A. Sharma, S. Wang, V. Pareek, H. Yang, D. Zhang, *Chem. Eng. Sci.* **2014**, *106*, 264.
- [35] H. Liu, A. Elkamel, A. Lohi, M. Biglari, *Ind. Eng. Chem. Res.* **2014**, *53*, 5554.
- [36] Y. Yang, Y. Xiang, G. Chu, H. Zou, B. Sun, M. Arowo, J. F. Chen, *Chem. Eng. J.* **2016**, *294*, 111.
- [37] Y. Zhang, X. Zhang, B. Xu, *Can. J. Chem. Eng.* **2016**, *93*, 2307.
- [38] Á. C. Varas, E. A. J. F. Peters, J. A. M. Kuipers, *Ind. Eng. Chem. Res.* **2017**, *56*, 5558.
- [39] S. M. H. Hashemi Amrei, S. Memardoost, S. Asadi, *Can. J. Chem. Eng.* **2015**, *92*, 1749.
- [40] J. Z. Luo, Y. Luo, G. W. Chu, *Chem. Eng. Sci.* **2016**, *155*, 386.
- [41] K. W. Chu, B. Wang, D. L. Xu, *Chem. Eng. Sci.* **2011**, *66*, 834.

Manuscript received January 17, 2018; revised manuscript received February 13, 2018; accepted for publication March 5, 2018.